Journal of The Electrochemical Society, **164** (6) A1037-A1049 (2017)
0013-4651/2017/164(6)/A1037/13/$37.00 © The Electrochemical Society

Electrochemical Cycle-Life Characterization of High Energy Lithium-Ion Cells with Thick $Li(Ni_{0.6}Mn_{0.2}Co_{0.2})O_2$ and Graphite Electrodes

Yongjun Leng,[a] Shanhai Ge,[b] Dan Marple,[a] Xiao-Guang Yang,[a] Christoph Bauer,[c] Peter Lamp,[c] and Chao-Yang Wang[a,*,z]

[a]*Department of Mechanical and Nuclear Engineering, and Electrochemical Engine Center (ECEC), The Pennsylvania State University, University Park, Pennsylvania 16802, USA*
[b]*EC Power, State College, Pennsylvania 16803, USA*
[c]*BMW Group, Munich, Germany*

A set of high-energy lithium-ion pouch cells consisting of thick $Li(Ni_{0.6}Mn_{0.2}Co_{0.2})O_2$ (NMC622) cathodes and thick graphite anodes were cycled under 1C-rate charge and 2C-rate discharge at room temperature. Fresh and cycle aged cells were characterized via various techniques, including cell capacity test, in-situ three-electrode cell and electrochemical impedance spectroscopy (EIS). The high-energy cells of ~200 Wh/kg studied have a cycle life of ~1419 cycles at capacity retention of ~75%. It is found that the capacity fade can be characterized into three stages: an initial stage of fast capacity drop, a second stage of gradual capacity loss, and a final stage of sharp capacity fade. The capacity fade is mainly due to loss of lithium inventory in the cells caused by growth of SEI layer during the initial and secondary stages and lithium plating during the final stage. Power fade of the cells is mainly due to the degradation of NMC622 cathode including the growth of surface film on NMC622 electrode active materials and the increase in its charge-transfer resistance. In addition, the power fade exacerbates the cell's capacity fade at low temperatures.

Manuscript submitted December 28, 2016; revised manuscript received March 6, 2017. Published March 21, 2017.

Lithium ion batteries are considered one of the promising power systems for plug-in and pure electric vehicles (EV) due to their relatively high energy and high power densities.[1] In order to further increase the driving range of electric vehicles, it is desirable to improve the energy density of Li-ion batteries. There are two ways to improve the energy density of Li-ion batteries: improve and utilize high-capacity electrode materials, such as Ni-rich $Li(Ni_xMn_yCo_z)O_2$ (NMC) ($x+y+z = 1$, $x \geq 0.5$) layered oxides[2–5] and Li-rich layered oxides[6,7] used as positive electrode materials, Si-based composites[4,6] and Li metal[8,9] used as negative electrode materials; and increase the portion of active electrode materials contributing to the cell energy while minimizing the portion of non-active components, such as separators and current collecting foils, through optimization of cell design.[10–12] In the latter category, high active material loading or thick electrode is a major direction. In the present paper, Li-ion batteries with thick graphite anodes and thick Ni-rich NMC cathodes will be explored for near-term EV batteries.

Cycle life is a major limitation for ultra-thick electrodes in high energy density batteries, among other concerns of power density, low temperature performance and fast-charging capability.[10] For EV applications, the battery should last for more than 10 years for customer acceptance. In the past two decades, extensive effort has been made to improve the cycle life of Li-ion batteries and understand their degradation mechanisms, especially for high power Li-ion batteries.[13–18] Capacity fade and power fade have been reported to be two main types of degradation of Li-ion batteries.[17,18] There are several main factors associated with the capacity fade of Li-ion batteries including the formation/growth of the SEI layer on the graphite anode/electrolyte interface,[13,14,19] the loss of active electrode materials due to structural and chemical instability (e.g. volume change, phase transition, and dissolution),[14] and Li plating at low temperature or over-charge conditions.[13,14,20,21] These processes lead to the consumption of lithium inventory, and thus a decrease in cell capacity. The power fade of Li-ion batteries is mainly associated with the internal impedance rise. A lot of factors are attributed to the cell impedance rise including the formation/growth of the SEI layer on graphite anode/electrolyte interface,[13,14,19] the formation/growth of passivation layers at cathode/electrolyte interface,[13,14] the loss of the contact between cell components,[14] the reduction of the conductivity of polyvinylidene fluoride (PVDF)-carbon composite binder,[22] and the reduction of electrolyte conductivity caused by the electrolyte decomposition.[14] Moreover, power fade of Li-ion batteries will lead to an additional capacity fade by lowering the operating voltage range. The degradation mechanisms of Li-ion batteries also depends on the cell chemistry,[17,23] electrode structure, and operating conditions.[20,24,25] For example, high energy Li-ion batteries with thick electrodes may age differently than high power counterparts with thin electrodes. However, there are few reports on the investigation of degradation mechanisms for thick-electrode, high-energy Li-ion batteries in the literature.

$Li(Ni_{1/3}Mn_{1/3}Co_{1/3})O_2$ (NMC111) has already been commercialized for EV applications due to its relatively high capacity, low cost and excellent safety characteristics.[3] However, its specific capacity is only 150~160 mAh/g, which is still not high enough for next-generation EV applications.[3] Ni-rich NMC layered oxides can deliver higher capacity than NMC111 and potentially increase the energy density of lithium ion batteries. However, with increasing Ni content, Ni-rich NMC shows worse rate capability and poor stability. Great effort has been made to improve the stability and cycle life of Ni-rich NMC materials. For example, the stability and cycle life of Ni-rich NMC materials can be improved by surface modification/coating,[26,27] core-shell structure[28,29] and concentration-gradient structure.[5,30,31] Most of the work on the evaluation of the cycle life of Ni-rich NMC materials has been done in either coin cells[3,5,31] or small pouch cells,[5] and little work about the cycle life of Ni-rich NMC in large-format pouch cells has been reported in the literature.[10]

In this work, a set of high-energy pouch cells consisting of thick $Li(Ni_{0.6}Mn_{0.2}Co_{0.2})O_2$ (NMC622) cathodes and thick graphite anodes are cycled under 1C-rate charge and 2C-rate discharge at room temperature. Fresh and cycle aged cells at different cycle numbers will be diagnosed in two-electrode and in-situ three-electrode cells.

Experimental

Cell fabrication.—We fabricated ~3.3 Ah pouch cells using $LiNi_{0.6}Mn_{0.2}Co_{0.2}O_2$ (Umicore) as positive electrodes and graphite (Nippon Carbon) as negative electrodes with 1.0 M lithium hexafluorophosphate ($LiPF_6$) dissolved in ethylene carbonate (EC) / ethyl methyl carbonate (EMC) (3:7 by wt) + 2 wt% vinyl carbonate (VC) as electrolyte (BASF). The negative-to-positive (N/P) capacity ratio was designed at 1.2. The pouch cells contained 14 layers of negative electrodes and 13 layers of positive electrodes. A Celgard-2325 separator, 25 μm in thickness, was used. The negative and positive

*Electrochemical Society Member.
[z]E-mail: cwx31@psu.edu

electrodes were fabricated using the same method as reported by our group before.[32,33] The loadings of NMC622 in the positive electrode and graphite in the negative electrode were ∼19.4 and ∼12.1 mg/cm^2, respectively; and the total thickness of the double-sided positive and negative electrodes (including Al or Cu foil) was ∼149 and ∼175 μm, respectively. The designed reversible capacity based on the total positive electrode area was ∼3.1 mAh/cm^2. Each pouch cell had a 81 mm × 55 mm footprint area, weighed 64.5 grams, and had a 3.3 Ah nominal capacity (related to which all C-rates in this work are given) with specific energy greater than 200 Wh/kg estimated at a size of 10 Ah or larger. In this work, all cells are high energy pouch cells with thick NMC622 and thick graphite electrodes otherwise specifically stated.

Initial screening.—After a formation process, about 20 pouch cells were screened. An initial rate capability test of all fresh pouch cells was performed at room temperature to examine the discharge capacity as a function of discharge C-rate. A multi-channel Arbin battery testing system (Model: BT 2000 with 32 channels, Arbin Instruments, USA) was used for the initial rate capability test. The initial rate capability test included five charge/discharge cycles with the same charge process and five different discharge C-rates: C/3, 1C, 2C, 3C and 5C. First, the pouch cells were charged using a constant current/constant voltage (CC/CV) protocol, i.e. the cells were charged at 1C-rate current to 4.2 V, and then were held at 4.2 V until the measured current dropped to C/20-rate. After resting for 30 min, the cells were discharged until the cutoff voltage of 2.8 V was reached. After the initial performance check, 10 "very similar" cells were selected for cycle aging test. We assume that the cells with close discharge capacities under the same C-rate and similar high-frequency resistances (HFR) are "very similar". C/3 and 1C discharge capacity of these selected 10 cells deviate from average discharge capacity of all manufactured cells by +1.30%/−1.22% and +1.44%/−2.13%, respectively.

Cycle aging tests.—Cycle aging tests of the 10 pouch cells were performed using a multi-channel LAND instrument battery testing system (Model CT2001B-5V-10A, Land Instruments, China) at room temperature. The test protocol for each cycle included five steps: (1) a charge to 4.2 V at a 1C-rate, (2) a charge at a constant voltage of 4.2 V until the measured current dropped to C/10-rate, (3) a rest for 5 minutes, (4) a discharge to 2.8 V at a 2C-rate, and (5) a rest for another 5 minutes before going to the next cycle. When the cells reached a specific cycle number (for example, 300, 500, 1000 and 1500 cycles, etc.), the cycle aging test of one of the cells was stopped. Finally, 10 aged cells at varying cycle numbers were obtained. Please note that in this work, all aged cells refer to the cells that have been aged by cycling.

Diagnostic tests.—Two electrode and in-situ three-electrode diagnostic tests for the fresh and aged cells were performed to examine the cell performance decay and identify degradation mechanisms. In the literature, post-mortem analysis of aged Li-ion batteries as a very useful ex-situ method is often used to obtain chemical, structural and electrochemical change of electrode materials upon aging and identify the factors for the degradation.[16,20,34–36] For electrochemical post-mortem analysis, re-constructed coin cells including half-cells and 3-electrode full cells with a Li reference electrode were fabricated from selected parts of aged electrodes. This kind of ex-situ electrochemical method allows us to obtain the electrochemical performance of the cell including remaining material capacity as well as impedance of aged positive and negative electrodes, respectively. However, during the reconstruction process, the interface between electrode and electrolyte and electrode microstructure may change. In this work, we will use an in-situ three-electrode method developed by our group[17] to measure positive and negative electrode potentials along with full cell voltage during the charge/discharge performance test, and also measure the impedance of the individual electrodes and full cell. This in-situ three-electrode method does not change the interface between electrode and electrolyte and electrode microstructure, and also provides a way to obtain the electrochemical performance and impedance of individual electrodes for whole cells.

For the three-electrode diagnostic tests, a fully discharged cell (discharged to 2.7 V at 0.1C-rate) was partially opened along the edge of one side in an argon filled glove box and then assembled into a fabricated three-electrode cell holder with a lithium-metal reference electrode. The three-electrode cell holder was fabricated based on our previous design,[17] which was modified in order to fit the size and shape of the pouch cells used in this work. The pouch cell was placed in the three-electrode cell holder, which was filled with the same fresh electrolyte solution as that for fresh cells. A copper wire with one end flattened was fitted in polyethylene tubing, and a piece of lithium metal was cold-welded to the flat surface to form a lithium reference electrode.[17] The other end of the copper wire was used as an electrical contact with a cable. The lithium reference electrode was then inserted into the fitting in the cell holder. Two terminals were inserted into the fittings in the cell holder and tightly contacted the positive electrode tab as positive voltage and current probes, while another two terminals were inserted into the fittings in the cell holder and tightly contacted the negative electrode tab as negative voltage and current probes.

Two-electrode diagnostic tests included rate capability tests at room temperature, 1C discharge capacity tests at three different temperatures (40/0/−10°C), and impedance tests at room temperature. A multi-channel Arbin battery test system (Model: BT 2000, Arbin Instruments, USA) and a Modulab electrochemical test system (Solartron analytical, United Kingdom) were used for the capacity and impedance tests, respectively. An environmental chamber was used to control different ambient temperatures for the diagnostic test, except for room temperature. The test protocol for the capability test of aged cells was the same as that for initial rate capability test of fresh cells. For the capacity tests at different ambient temperatures, the cells were fully charged using CC (1C-rate)/CV (4.2 V) charging protocol at room temperature, and then the cells were discharged at required ambient temperature until a cutoff discharge voltage of 2.8 V was reached. For impedance tests at room temperature, the cells were fully charged and then discharged to ∼90% SOC at C/2-rate. After the cells were balanced for at least two hours at ∼90% state of charge (SOC), impedance test was performed with an AC voltage amplitude of 5 mV in the frequency range of 50 kHz to 0.005 Hz.

Three-electrode diagnostic tests included rate capability test at 25°C and impedance tests at two different ambient temperatures (25 and −10°C). The three-electrode diagnostic tests were performed for a fresh and two selected aged cells. The Arbin tester was used for the three-electrode rate capability tests at 25°C. The test protocol for three-electrode rate capability tests was the same as for the two-electrode rate capability tests. During the three-electrode rate capability tests, two auxiliary channels were used to simultaneously record the positive and negative electrode potentials. A Modulab electrochemical test system combined with an environmental chamber was used to perform the impedance tests. For the impedance tests, the cells were fully charged using CC (C/2-rate)/CV (4.2 V) charging protocol, and then were discharged to ∼80% SOC using a C/2-rate at 25°C. After the cells were balanced at ∼80% SOC and required ambient temperature for at least four hours, impedance tests were performed for full cell, positive electrode and negative electrode in the frequency range of 50 kHz to 0.005 Hz.

Results and Discussion

Beginning-of-life (BOL) performance.—Figure 1a shows the discharge performance as a function of C-rate for a fresh cell at room temperature. The cell can achieve a C/3 discharge capacity of 3.20 Ah and a C/3 discharge energy of 11.65 Wh, which corresponds to a Coulombic efficiency of ∼ 99.3% (vs. a charge capacity of 3.22 Ah) and an energy efficiency of ∼ 91.9% (vs. a charge energy of 12.67 Wh). If extrapolating the same electrodes and cell components to a 10 Ah or larger cell, the cell energy density can reach >200 Wh/kg. One can also find that the rate capability of the fresh cell is very poor, which

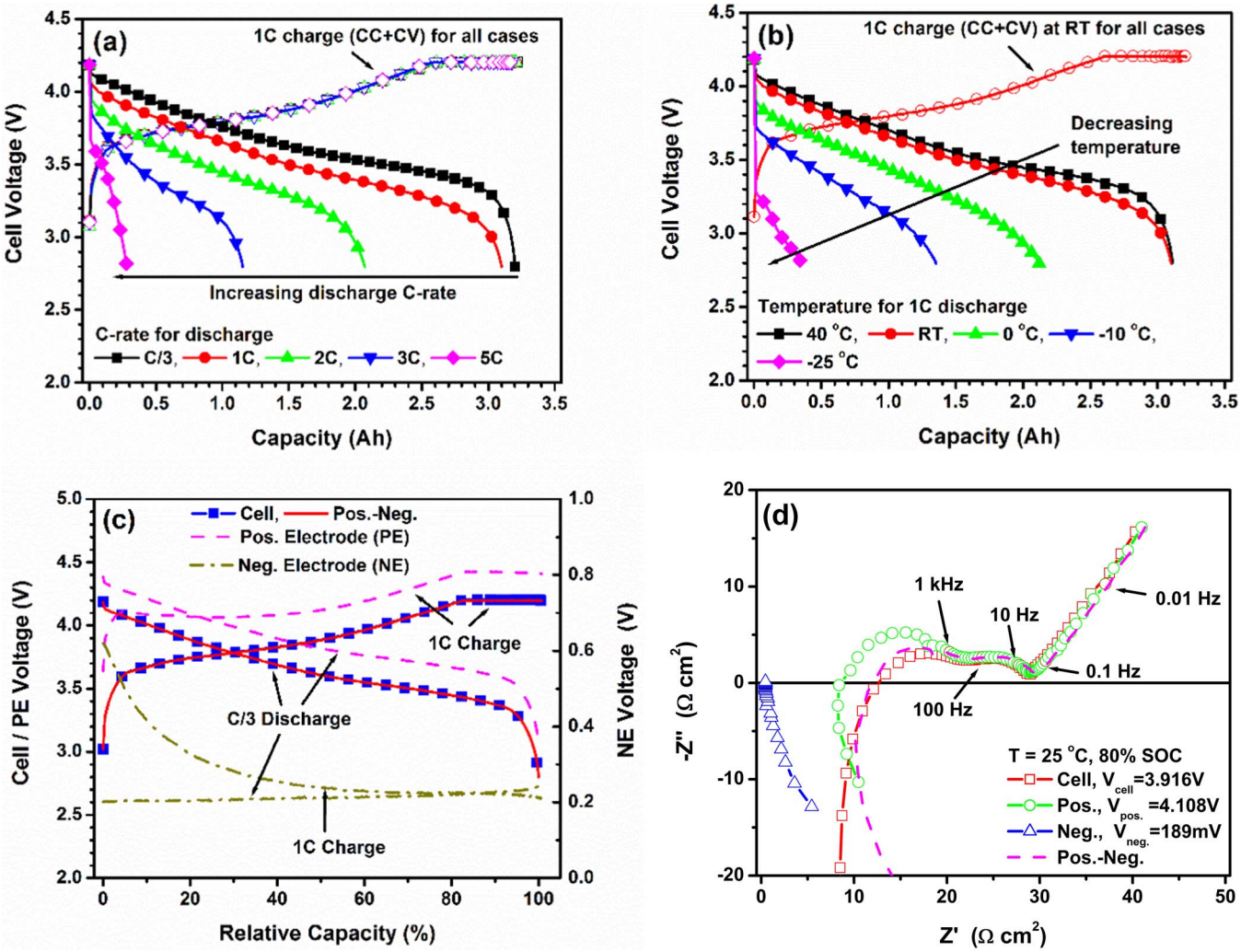

Figure 1. Beginning-of-Life (BOL) performance of a high energy NMC622/graphite cell with 200 Wh/kg: (a) discharge performance under different C-rate at room temperature (~23°C); (b) temperature effect on 1C discharge performance; (c) separation of positive and negative electrode potentials from full cell voltage in a three-electrode cell during 1C charge-C/3 discharge process at 25°C (Note: Capacity is normalized based on the C/3 discharge capacity measured in a three-electrode cell: 3.17 Ah); (d) separation of positive and negative electrode impedance from whole cell impedance in a 3-electrode cell at 25°C (Note: impedance has been normalized based on total positive electrode area of 1055 cm^2).

is typical for a high energy cell. For example, at room temperature, the discharge capacities under 1C, 2C, 3C and 5C are 3.10, 2.07, 1.15 and 0.28 Ah, which are 96.9%, 64.7%, 35.9% and 8.8%, respectively, of the C/3 discharge capacity. It is believed that the poor rate capability for a high energy cell is related to high internal cell resistance due to large resistance for Li ion transport within the thick electrodes. For a high energy cell, low temperature performance is also poor, as shown in Figure 1b. At 0, −10 and −25°C, the cell can deliver 1C discharge capacities of 2.12, 1.35 and 0.35 Ah, which are corresponding to 68.4%, 43.5%, and 11.3% of the 1C discharge capacity at room temperature, respectively. The poor performance at low temperatures for a high energy cell is attributed to reduced conductivity of the electrolyte through the separator and inside the thick electrodes, limited lithium solid diffusivity in the electrode material particles and significantly increased charge-transfer resistance on the electrolyte-electrode interface.[37,38] In addition, with increasing temperature from room temperature (~23°C) to 40°C, 1C discharge performance improves slightly. In order to separate positive and negative electrode contributions from the full cell performance, the measurement of the capacity and impedance in a three-electrode cell was performed, as shown in Figures 1c and 1d, respectively. From Figure 1c, one can find that the difference between the positive and negative electrode potentials is almost the same as the full cell voltage at the same relative capacity (i.e. depth of discharge, DOD). In addition, the cell measured in a three-electrode cell can deliver a C/3 discharge capacity and energy of ~3.17 Ah and ~11.58 Wh, respectively, which are almost the same as those measured in a two-electrode cell (Figure 1a). Moreover, the profile of the positive and negative electrode potentials as functions of DOD is consistent with the results for either half-cells or full cells with Li reference electrodes as reported in the literature.[17,39,40] The results shown in Figure 1c implies that our three-electrode method can be used to effectively separate the positive and negative electrode potentials from full cell voltage during charge-discharge cycle, and the installation of Li reference electrode has no negative effect on the measurement of full cell voltage or cell charge/discharge capacity and energy. Moreover, as evidenced by Figure 1d, the sum of the positive and negative electrode impedances is almost the same as full cell impedance in the frequency range from 1 kHz to 0.005 Hz. However, there is some deviation of the sum of the positive and negative electrode impedance from the full cell impedance in the very high frequency range (>1 kHz), which is due to the different effects of inductance behavior on the positive/negative electrode and full cell impedances. In addition, at 25°C, the cell impedance at 80% SOC is dominated by the positive electrode impedance, while the negative

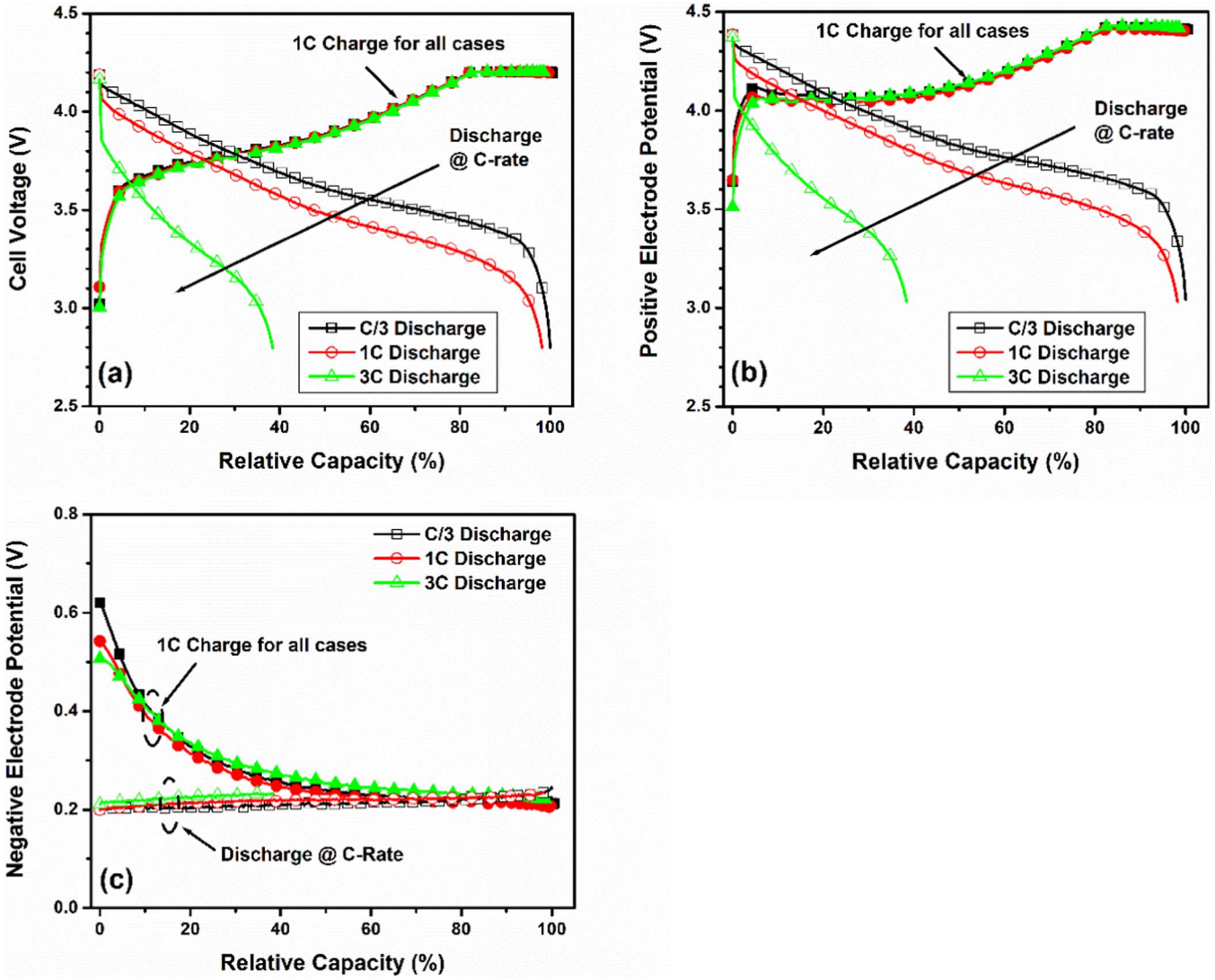

Figure 2. Effect of C-rate on (a) full cell voltage, (b) positive and (c) negative electrode potentials during 1C charge-C/3 discharge process for a fresh high energy NMC622/graphite cell at 25°C. (Note: Capacity is normalized based on the C/3 discharge capacity of 3.17 Ah measured in a three-electrode cell).

electrode impedance is quite small. This implies that the rate capability of a high energy cell mainly depends on the positive electrode.

Figure 2 shows the effect of C-rate on full cell voltage and positive and negative electrode potentials as functions of relative capacity measured in a three-electrode cell during 1C charge-C/3 discharge process for a fresh cell at 25°C. Capacity was normalized based on the C/3 discharge capacity of 3.17 Ah measured in the three-electrode cell. It is confirmed that for a high energy cell, rate capability of the cell mainly depends on the positive electrode. At 25°C, since the kinetics of graphite negative electrode are fast, the negative electrode potential changes slightly with increasing C-rate from C/3 to 3C. Moreover, due to the sluggish kinetics of the NMC622 positive electrode, the decrease in full cell voltage with increasing C-rate mainly comes from the decrease in the positive electrode potential. This result is consistent with the three-electrode impedance test shown in Figure 1d.

Capacity fade.—The change of C/3 discharge capacity and capacity retention upon cycling is used to describe the capacity fade with cycle aging. Capacity retention is defined as the ratio of the discharge capacity of an aged cell at a certain cycle number to that of a fresh cell. Figure 3 shows 1C charge-C/3 discharge curves and C/3 capacity retention as a function of cycle number for the cells. During the initial stage (within 313 cycles), there is ∼10% loss in the C/3 discharge capacity, while almost no power fade is observed. During the secondary stage (from 313 to 1000 cycles), there is gradual capacity loss and power fade with cycle number. The capacity retention drops by ∼2.3% (from 90.0 to 87.7%) from 313 to 1000 cycles. However, after 1000 cycles (final stage), the capacity decay becomes fast and power fade becomes significant. The decay rate in the C/3 capacity retention during initial, secondary, and final stages is 3.19%, 0.33% and 3.46% per 100 cycles, respectively. In the case of C/3 discharge performance, there is almost no effect of power fade on the capacity fade since the aged cell capacity is still limited by a diffusion process. We will focus on capacity fade in this section and discuss power fade later.

For a comparison, another batch of pouch cells with thick NMC111 (Umicore) cathodes and thick graphite anodes were fabricated with the same procedure. The NMC111/graphite cells have similar electrode thickness, loading and cell size to NMC622/graphite. C/3 capacity retention at room temperature as a function of cycle number of NMC111/graphite cells is shown in Figure 3b. The trend in the capacity decay with cycle number for the NMC111/graphite cells is similar to that for the NMC622/graphite cells. Since NMC622 materials are less stable than NMC111,[3] cycle life for the NMC622/graphite cells is shorter than that for the NMC111/graphite cells (1419 vs. 1860 cycles with capacity retention of 75%) as expected. This implies that the NMC622/graphite cells have similar degradation mechanisms to

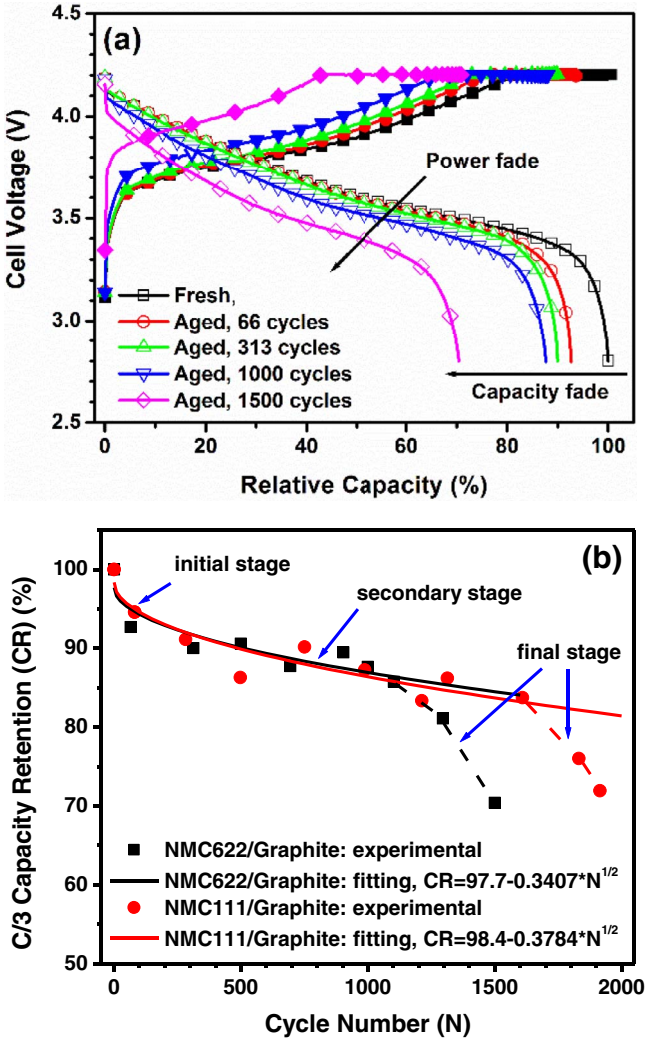

Figure 3. (a) 1C charge and C/3 discharge curves of aged cells (Note: Capacity is normalized based on the C/3 discharge capacity of 3.20 Ah for a fresh cell), and (b) C/3 capacity retention (CR) at room temperature (~23°C) as a function of cycle number (N) for high energy NMC622/graphite cells. For comparison, C/3 capacity retention at room temperature as a function of cycle number for NMC111/graphite cells with similar electrode thickness, loading and cell size fabricated with the same procedure is also shown in Figure 3b.

the NMC111/graphite cells. In the literature, the degradation mechanisms for lithium ion cells with NMC111,[41–43] $Li(Ni_{0.5}Mn_{0.3}Co_{0.2})O_2$ (NMC532),[44] NMC111/$LiMn_2O_4$ blend,[16,20] and NMC532/$LiMn_2O_4$ blend[45] cathodes have been relatively well documented. That is, the capacity fade is mainly attributed to the loss of lithium inventory caused by SEI layer formation/growth at the anode, and loss of active materials at the cathode. Similar degradation mechanisms have also been proposed for Li-ion cells with other cathode materials.[14,19,34,46] For example, Snyder et al.[19] found that the entirety of capacity loss up to 80 cycles in $LiCoO_2$/graphite cells can be attributed to the loss of lithium inventory caused by SEI formation and repair. Due to similarity between NMC622 and other NMC materials, for the NMC622/graphite cells studied in this work, the sharp decrease in C/3 capacity retention during the initial stage is considered to be due to the loss of lithium inventory caused by the quick growth of solid-electrolyte interphase (SEI) layer on the graphite negative electrode.[43–45,47,48] Gradual decrease in C/3 capacity retention during the secondary stage is attributed to continuously slow growth of the SEI layer on the graphite negative electrode.[43–45,47,48] As shown in Figure 3b, for both NMC662/graphite and NMC111/graphite pouch cells, the decrease in capacity retention (CR) with cycle number (N) during the initial and secondary stages depends on the square root of cycle number ($N^{1/2}$), which agrees with parabolic model of capacity fade due to SEI layer growth on negative electrode.[48–50] During the final stage, there is a significant drop in C/3 capacity retention, which deviates from the extension of the trend in the capacity fade with cycle number during the initial and secondary stages. This implies that besides the growth of SEI layer, there is another factor contributing to the significant loss of lithium inventory and severe capacity fade during the final stage, which is believed to be due to lithium plating. Lithium plating has been considered as one of the main reasons attributed to the abrupt capacity fade during the final stage in the literature.[10,13,23,24,34,42] For example, Schuster et al.[24] reported that the abrupt capacity fade after the "turning point" from linear to non-linear aging characteristics is due to *aging induced lithium plating*, which may originate from reduced ionic kinetics of the graphite negative electrode as a result of SEI growth and the loss of graphite active materials. Burns et al.[42] believed that electrolyte oxidation products are produced at the positive electrode and migrate to the negative electrode where they are reduced as a solid layer of unwanted materials on the front surface of the negative electrode; moreover, after a sufficient number of cycles the layer of unwanted materials becomes thick enough to significantly reduce ion transport to the bulk of the negative electrode, which leads to large kinetic issues when trying to cycle the cell and subsequent lithium plating. Gallagher et al.[10] observed obvious Li deposits on graphite anode for cycled NMC622/graphite pouch cells, especially for the cells with high loading active materials (i.e. areal capacity $\geq$3.3 mAh/cm^2); and found that Li deposit associated with lithium plating dramatically increases with increasing electrode thickness. Similarly, in this work, for the pouch cells with thick electrode, since the areal capacity is as high as ~3.1 mAh/cm^2, the cells tend to lithium plating during the final stage.

Power fade.—Figure 4a shows 1C charge-1C discharge performance of fresh and aged cells at room temperature. One can find that within 313 cycles, there is almost no power fade in the case of 1C discharge and cell performance decay is mainly the capacity fade. However after 313 cycles, there is a significant power fade upon further cycle aging, especially from 904 to 1500 cycles. In order to identify whether the power fade comes from either the positive or negative electrode, three-electrode diagnostic tests were performed for a fresh and two aged cells with 904 and 1500 cycles. Figures 4b, 4c and 4d show full cell voltage, positive and negative electrode potentials, respectively, as a function of discharge capacity during the 1C discharge process for fresh and aged cells at 25°C. It is noted that the performance of the aged cell at 1500 cycles improves when it was measured in a three-electrode cell, compared with a two-electrode cell. This kind of performance improvement is due to the reduction in contact resistance and the use of fresh electrolyte solution in the three-electrode cell. We will discuss this issue in detail later. Table I summarizes the average full cell voltage and positive and negative electrode potentials measured in a three-electrode cell during 1C discharge step at 25°C. In the case of 1C discharge, the power fade of the cell upon aging mainly comes from the positive electrode. For example, after cycle aging for 904 cycles, the average full cell voltage decreases by ~91 mV, which mainly comes from the decrease in the average positive electrode potential (~93 mV), while the average negative electrode potential changes minimally. After cycle aging for 1500 cycles, the average positive electrode potential decreases by ~181 mV, while the average negative electrode potential decreases by ~19 mV. This implies that the power performance of positive electrode is worsen, while that of negative electrode is improved. The improvement in the performance of negative electrode may be related to increased electrochemical reaction area of negative electrode materials caused by the dramatic crack propagation of graphite negative electrode materials, as to be confirmed by three-electrode impedance tests at −10°C later. Therefore, the average full cell voltage decreases by ~162 mV, which also mainly comes from the positive electrode.

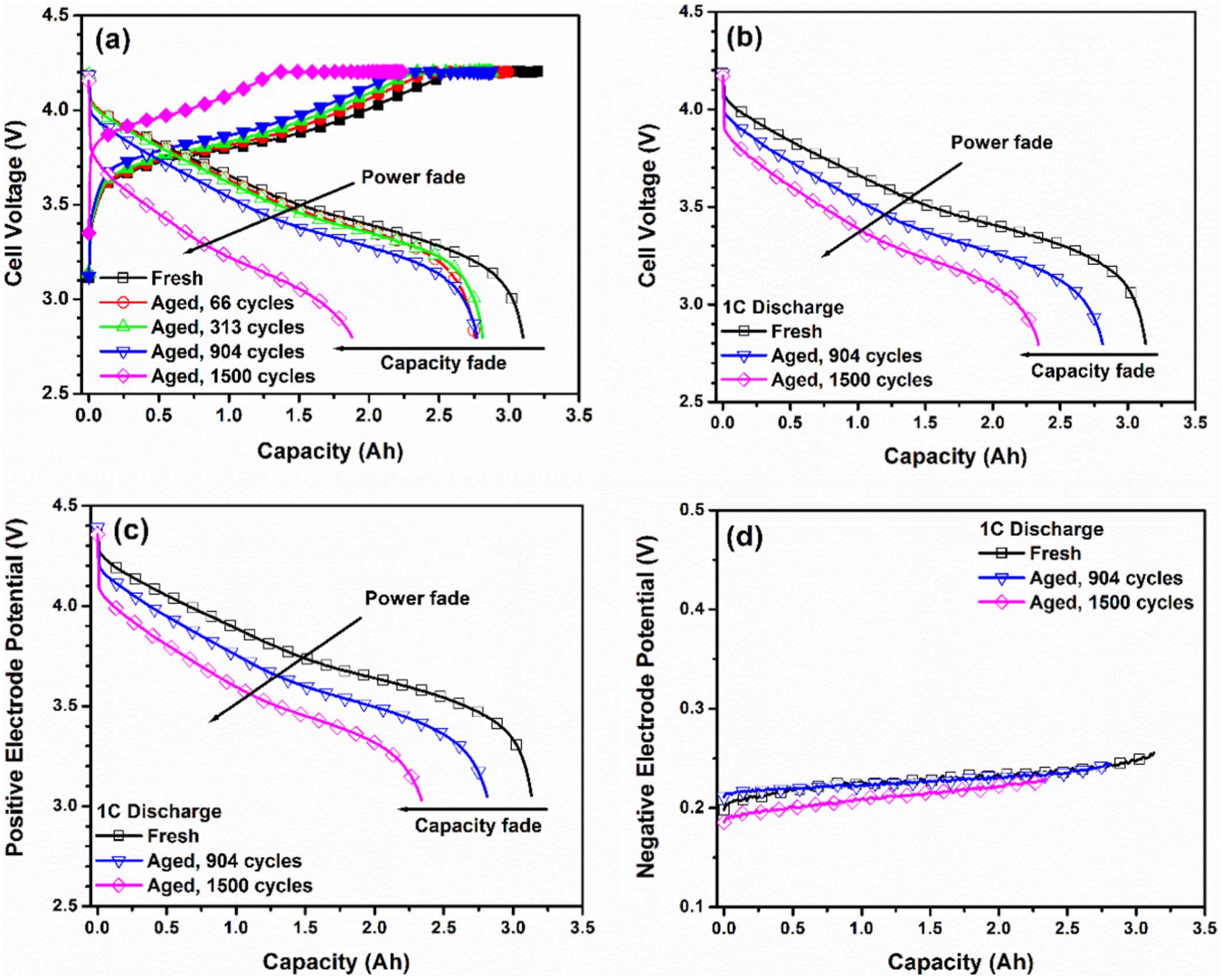

Figure 4. 1C charge/1C discharge performance of aged cells measured in (a) a two-electrode cell at room temperature (~23°C) and (b, c, d) a three-electrode cell at 25°C. In three-electrode diagnostic test, (b) full cell voltage, (c) positive and (d) negative electrode potentials as a function of discharge capacity were measured simultaneously during the discharge process.

Generally, power fade of a Li-ion cell upon aging is directly related to the impedance rise of the cell. In order to identify the degradation mechanism for the cell power fade, the impedance of fresh and aged cells was measured at 90% SOC and room temperature in a two-electrode cell, as shown in Figure 5a. For most of the aged cells (at ≥313 cycles), there are two obvious arcs located in the high-frequency and medium-frequency regions, followed by a Warburg diffusion impedance (a straight line) located in low-frequency region. While for the fresh cell and aged cell at 66 cycles, the two arcs in the high- and medium- frequency regions are overlapped. From the impedance test of a fresh cell (Figure 1d) and that for aged cells at 904 and 1500 cycles in a three-electrode cell, Figure 6, it was confirmed that the full cell impedance mainly comes from the positive electrode. The high-frequency arc is attributed to the migration of Li ions through the surface film formed/grown on the positive electrode active materials[41,51,52] and/or electronic transport in the electrode,[53,54] while the medium-frequency arc is related to the charge-transfer reaction (mainly positive electrode).[51,52,54] The Warburg diffusion impedance in the low-frequency region is related to Li solid diffusion in the active materials and electrolyte salt diffusion process. An equivalent circuit with two time constants (Figure 5b) was proposed and used to fit the experimental impedance data in the high- and medium-frequency region. In the equivalent circuit, L is the high-frequency inductance due to cable wires; R_{ohm} is ohmic resistance from the electrodes, electrolyte, separator, current collector and the contact between cell components; CPE_1 and R_1 are constant-phase-element (CPE) and

Table I. Average full cell voltage, positive and negative electrode potentials measured by a 3-electrode cell during 1C discharge of fresh and aged high energy NMC622/graphite cells at 25°C.

Cycle number	Average full cell voltage (V)	Average positive electrode potential (V)	Average negative electrode potential (V)
fresh	3.527	3.754	0.229
904 cycles	3.436	3.661	0.227
1500 cycles	3.365	3.573	0.210

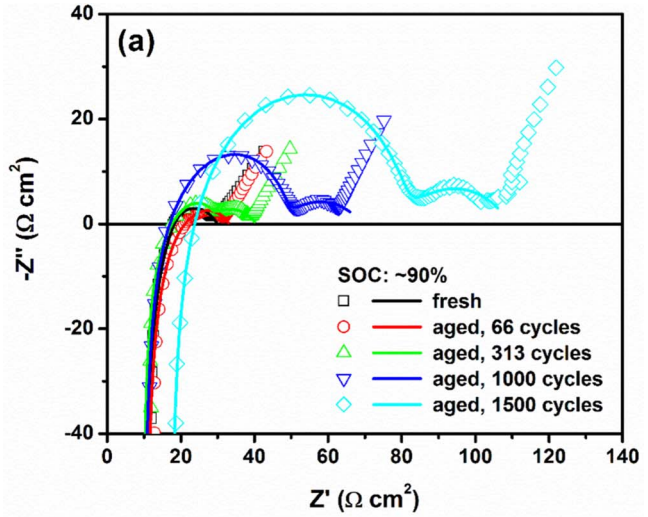

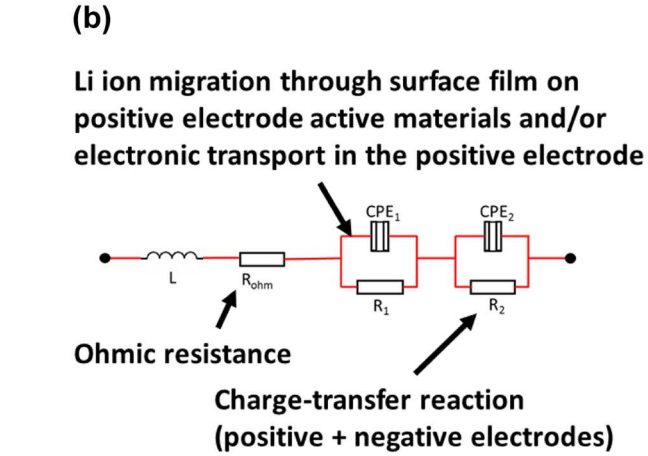

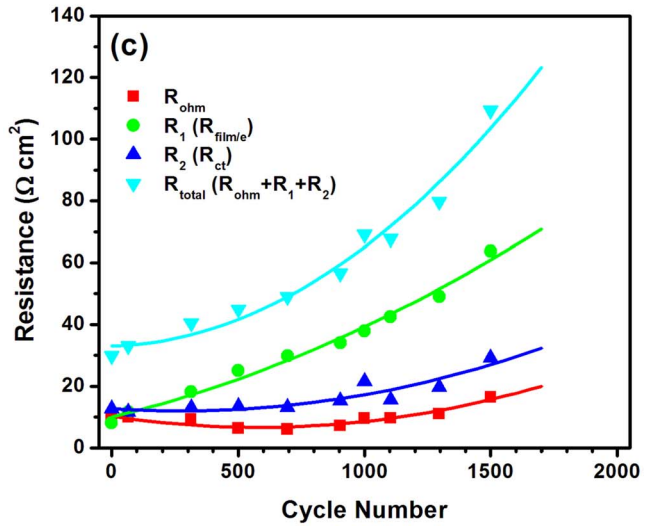

Figure 5. (a) Cell impedance of a fresh and selected aged cells measured at 90% SOC and room temperature using two-electrode cell (symbols: experimental data, lines: fitted), (b) An equivalent circuit used for fitting cell impedance spectra shown in Figure 5a (Note: Warburg diffusion impedance showing a inclined line in the low frequency range isn't included in the equivalent circuit), (c) Evolution of resistances related to different processes as a function of cycle number at room temperature for high energy NMC622/graphite cells. (Note: impedance has been normalized based on total positive electrode area of 1055 cm^2).

Table II. Fitting parameter values for the impedance spectra (excluding diffusion line part) of a fresh and selected aged cells measured under 90% SOC at room temperature using two-electrode configuration shown in Figure 5a.

Cycle No.	fresh	66	313	1000	1500
L (mH cm^2)	0.315	0.341	0.243	0.305	0.293
Rohm (Ω cm^2)	9.17	9.97	9.30	9.54	16.4
R_1 (Ω cm^2)	8.06	11.6	18.2	38.0	63.8
CPE_1 A_1 (μF cm^{-2})	5.96	4.18	2.78	1.99	2.09
n_1	0.913	0.939	0.957	0.959	0.923
R_2 (Ω cm^2)	12.7	11.6	13.0	21.6	29.2
CPE_2 A_2 (mF cm^{-2})	2.66	4.82	6.96	11.6	7.21
n_2	0.561	0.526	0.504	0.472	0.541
R_{total} (Ω cm^2)	29.9	33.1	40.5	69.1	109.3

resistance related to the surface film and/or electronic transport in the positive electrode, respectively; and CPE_2 and R_2 are the CPE and charge-transfer resistance related to the charge-transfer reaction at the electrodes (the positive electrode mainly), respectively. The impedance of CPE is defined by the equation: $Z_{CPE} = A/(j\omega)^n$, where j is the complex number, ω is the angular frequency, and A is the coefficient of the impedance of CPE. The fitting parameter values for the cell impedance of fresh and aged cells at 90% SOC and room temperature are summarized in Table II. The experimental impedance spectra of the cells and the fitted ones show good agreement for all fresh and aged cells, as illustrated in Figure 5a. Figure 5c shows the evolution of resistances related to different processes as a function of cycle number at room temperature for the cells. The ohmic resistance (R_{ohm}) and charge-transfer resistance (R_2) are both nearly constant within 1000 cycles, and they gradually increases with cycle number after 1000 cycles. The resistance R_1 significantly increases with increasing cycle number from 0 to 1500 cycles, which results from growth of surface film on the positive electrode active materials. After 313 cycles, the contribution of the resistances to the total cell resistance is in the order: resistance related to the surface film/electronic transport (R_1) > charge-transfer resistance (R_2) > ohmic resistance (R_{ohm}), and the contribution of R_1 becomes larger with more cycles. The total cell resistance (R_{total}), the sum of R_1, R_2 and R_{ohm}, significantly increases with cycle number. For example, for an aged cell at 1500 cycles, the total cell resistance is ~109 Ω cm^2, more than three times that for a fresh cell (~30 Ω cm^2). Great increase in the cell resistance upon aging leads to a significant power fade, as shown in Figure 4.

Three-electrode impedance tests for fresh and aged cells were performed in order to explore how the change of the positive and negative electrode impedance upon aging affects the cell impedance rise. Figure 6 shows a comparison of the full cell, positive electrode and negative electrode impedances at 80% SOC and 25°C among fresh and two aged cells with 904 and 1500 cycles. One can find that the positive electrode dominates the full cell impedance, for both fresh and aged cells. Compared with the positive electrode impedance, the negative electrode impedance is small and can be neglected. The same equivalent circuit shown in Figure 5b was used to fit the cell and positive electrode impedance spectra (except for Warburg diffusion impedance in the low-frequency region) measured in a three-electrode cell. Please note that in the case of positive electrode impedance, R_{ohm} is ohmic resistance of a half-cell consisting of positive electrode, CPE_1 and R_1 are related to surface film on the positive electrode active materials and/or electronic transport in the positive electrode, and CPE_2 and R_2 are related to the charge-transfer reaction at the positive electrode. The experimental impedance spectra of the full cells and positive electrodes and the fitted ones show good agreement for the fresh and aged cells, as illustrated in Figure 6a and 6b. The fitting parameter values for the full cell and positive electrode impedance as a function of cycle number at 80% SOC and 25°C are summarized in Table III. Figure 7 shows a comparison in the resistance related to different processes fitted from the impedance test data (Figure 6a and 6b) between

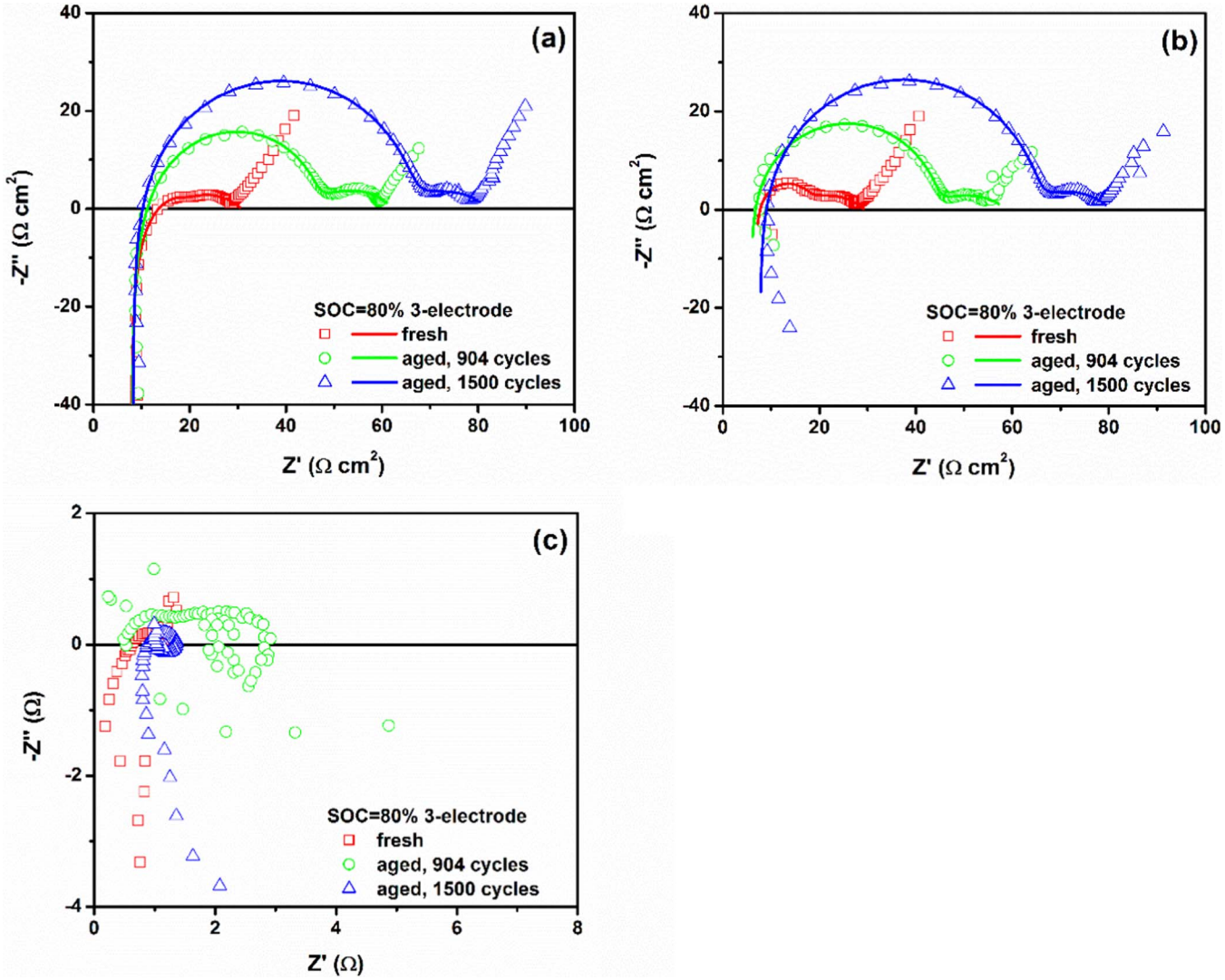

Figure 6. A comparison of (a) full cell, (b) positive electrode and (c) negative electrode impedance measured at 80% SOC and 25°C (symbols: experimental data, lines: fitted) in a 3-electrode cell among a fresh and two aged cells at 904 and 1500 cycles.

full cell and positive electrode at 25°C. For fresh and aged cells, the resistance R_1 and the charge-transfer resistance (R_2) for the positive electrode are almost the same as those for the full cell. Moreover, with increasing cycle number, the increase in R_1 and charge-transfer resistance (R_2) for the positive electrode impedance followed almost the same trend as that for the full cell. In addition, the rise in cell impedance upon aging mainly comes from the increase in the positive electrode impedance. These results imply that the power fade of the cell upon cycle aging is mainly due to the positive electrode including the increase in the resistance related to the surface film/electronic transport, and the increase in its charge-transfer resistance, which is consistent with the discharge performance of the full cell and the positive electrode measured in a three-electrode cell (Figure 4).

Performance fade at low temperature.—Figures 8a and 8b show 1C discharge performance of fresh and aged cells at 0 and −10°C,

Table III. Fitting parameter values for the impedance spectra (excluding Warburg diffusion impedance) of a fresh and two aged cells (at 904 and 1500 cycles) measured at 80% SOC and room temperature in a three-electrode cell shown in Figure 6a and 6b.

	Fresh		Aged, 904 cycles		Aged, 1500 cycles	
Cycle No.	cell	positive	cell	positive	cell	positive
L (mH cm^2)	0.123	0.017	0.128	0.031	0.108	0.071
Rohm (Ω cm^2)	7.26	6.47	7.62	5.57	7.86	7.41
R_1 (Ω cm^2)	9.65	8.68	38.1	37.7	56.8	56.9
CPE_1 A_1 (μF cm^{-2})	2.04	1.28	2.27	1.94	1.82	1.77
n_1	1.002	1.061	0.949	0.960	0.965	0.966
R_2 (Ω cm^2)	13.8	14.3	16.6	15.6	17.5	16.1
CPE_2 A_2 (mF cm^{-2})	3.23	2.93	9.19	15.7	10.8	10.8
n_2	0.485	0.465	0.526	0.444	0.466	0.512
R_{total} (Ω cm^2)	30.7	29.5	62.3	58.8	82.1	80.5

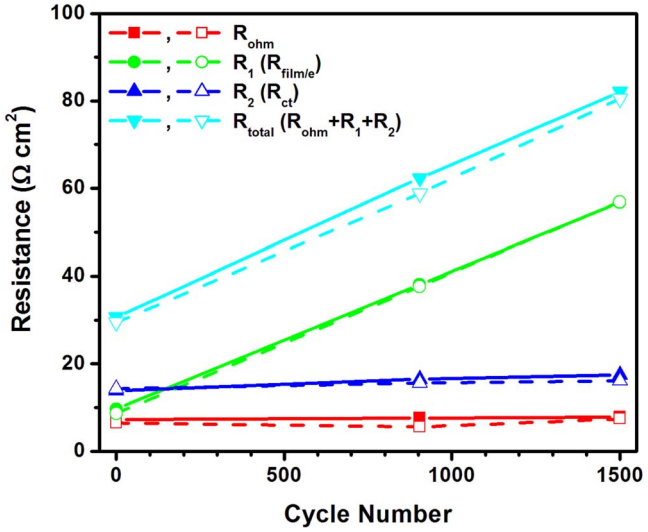

Figure 7. A comparison in the resistances related to different processes at 25°C between full cell (solid line + solid symbol) and positive electrode (dash line + open symbol) fitted from the impedance test data shown in Figure 6. (Note: impedance has been normalized based on total positive electrode area of 1055 cm^2).

respectively. Before the discharge, the cells are fully charged using CC (1C-rate) / CV (4.2 V) protocol at 25°C. At both 0 and −10°C, there is not only a significant capacity fade, but also a great power fade upon aging, especially from 1000 to 1500 cycles. Compared with the power fade at room temperature, the power fade at low temperatures becomes more significant. Figure 8c shows 1C discharge capacities as a function of cycle number at four different temperatures in the rage from 40 to −10°C. Generally, the capacity decay at lower temperature becomes faster, which is due to stronger effect of power fade on the 1C discharge performance.

In order to identify the source of the significant power fade at low temperatures, impedance tests using the three-electrode configuration was performed at −10°C for fresh and aged cells. Figure 9 shows a comparison of the full cell, positive electrode and negative electrode impedances at 80% SOC at −10°C for a fresh and two aged cells at 904 and 1500 cycles. In the case of full cell impedance (Figure 9a), there is an arc, a diffusion line, another arc and a short inclined line related to Warburg diffusion impedance located in the high, medium, low and extra-low frequency regions, respectively. Compared with the full cell impedance at 25°C (Figure 6a), an additional diffusion line appears in the medium-frequency region at −10°C. Since full cell impedance (real part and imaginary part) is theoretically the sum of positive electrode impedance and negative electrode impedance at every frequency, based on the analysis of the characteristic frequencies of the arcs and additional diffusion line that appeared in impedance spectra, it can be

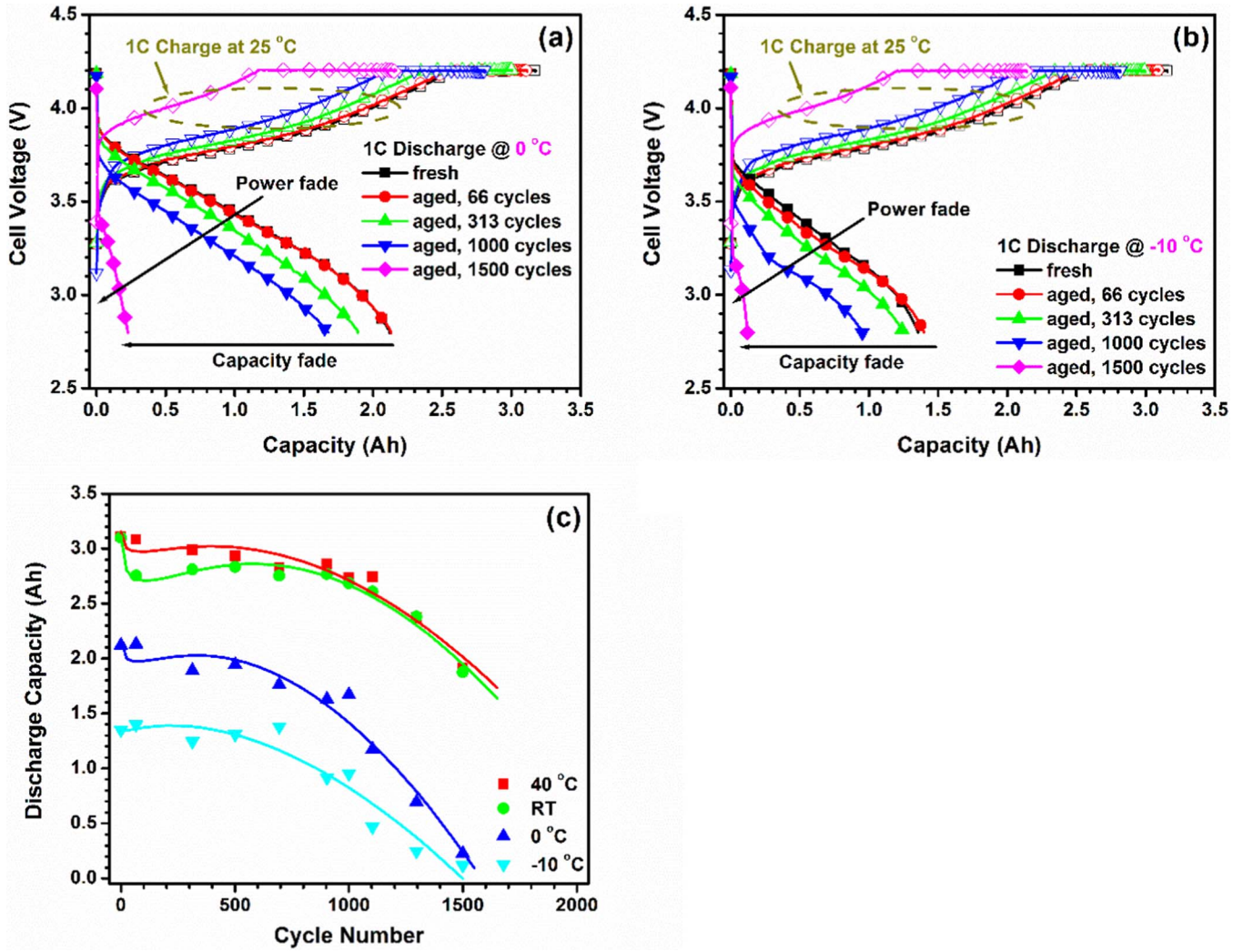

Figure 8. 1C charge curves at 25°C and 1C discharge curves at required ambient temperature (a) 0°C and (b) −10°C, of aged cells, and (c) 1C discharge capacity as a function of cycle number at four different temperatures in the range from 40 to −10°C for high energy NMC622/graphite cells.

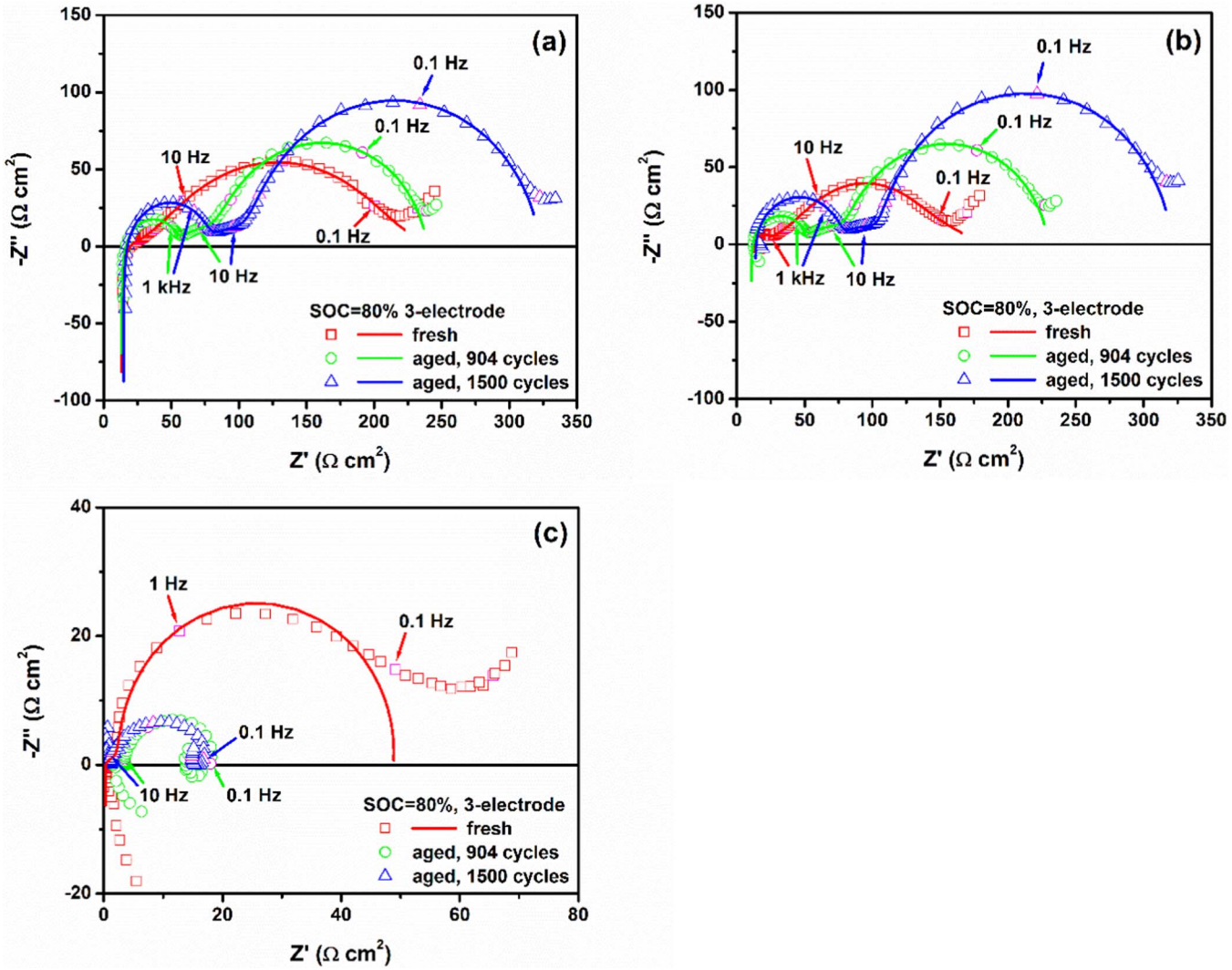

Figure 9. A comparison of (a) full cell, (b) positive electrode, and (c) negative electrode impedance measured at 80% SOC and −10°C (symbols: experimental data, lines: fitted) in a three-electrode cell among a fresh and two aged cells at 904 and 1500 cycles.

found that the high-frequency arc and the medium-frequency diffusion line of the full cell come from the positive electrode only; while for the low-frequency arc, it is contributed to by both positive and negative electrodes, especially for the fresh cell. When temperature is reduced from room temperature to −10°C, due to slow lithium solid diffusion process in the particles of the electrode active materials and sluggish electrolyte salt diffusion in the electrodes, Warburg diffusion impedance becomes very large and a line related to Warburg diffusion impedance needs to be captured in extremely low frequency region. In this work, Warburg diffusion impedance appears as a short inclined line at −10°C when frequency is swept to the low frequency limit of 0.005 Hz. In the case of positive electrode impedance at −10°C, similar impedance pattern to full cell impedance is observed. Like that at 25°C, the arcs in the high-frequency and the low-frequency region at −10°C are attributed to the Li ion migration through surface film formed/grown on the positive electrode active materials and the charge-transfer reaction, respectively, while the additional diffusion line in the medium-frequency region at −10°C may be due to the electronic transport in the positive electrode. Sun et al.[54,55] investigated the impedance of $LiMn_2O_4$ and $LiNi_{1/3}Co_{1/3}Mn_{1/3}O_2$ cathodes and observed a similar phenomenon. In their work, the author also claimed that the high-frequency depressed arc at room temperature includes the contribution of electronic transport in the electrode.[55] In the case of negative electrode impedance at −10°C, for a fresh cell, there is a small arc and a large arc in the high and low-frequency region, respectively, and an inclined line related to Warburg diffusion impedance in the extra-low frequency region; while for the two aged cells, the short inclined line related to Warburg diffusion impedance disappears. The high and low frequency arcs are attributed to the growth of solid-electrolyte interphase (SEI) layer and charge-transfer reaction at the negative electrode, respectively.[56] The short inclined line is due to slow lithium solid diffusion in graphite particles and electrolyte salt diffusion in the negative electrode.

Two different equivalent circuits, as shown in Figure 10, were proposed to fit the impedance data (except for the inclined line related to Warburg diffusion impedance), one for the full cell and positive electrode and one for the negative electrode. The equivalent circuit for the impedance spectra in the case of full cell and positive electrode consists of three different time constants besides an inductor L and an ohmic resistance R_{ohm}. Specifically, a constant-phase element (CPE) (CPE_{MF}) parallel with a resistance (R_{MF}) was used to fit the additional diffusion line in the medium-frequency region for better fitting. R_1 and CPE_1 for high-frequency arc are the resistance and corresponding capacitance related to surface film on the positive electrode active materials, R_{MF} and CPE_{MF} for the medium-frequency diffusion line are the resistance and corresponding capacitance related to electronic transport in the positive electrode, and R_2 and CPE_2 for the low-frequency arc are the charge-transfer resistance and double-layer

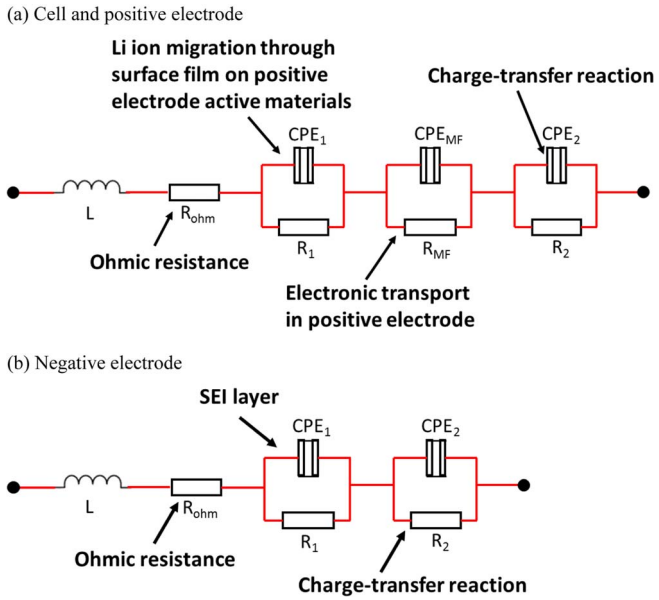

Figure 10. Equivalent circuits for (a) cell and positive electrode, and (b) negative electrode used to fit cell impedance spectra shown in Figure 9. (Note: Warburg diffusion impedance showing a short inclined line in the low frequency range isn't included in the equivalent circuits).

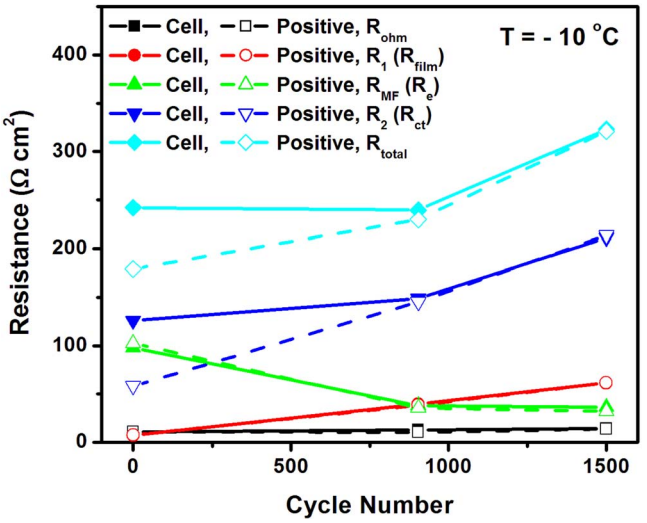

Figure 11. A comparison in the resistances related to different processes at −10°C between full cell (solid line + solid symbol) and positive electrode (dash line + open symbol) fitted from the impedance test data shown in Figure 9. (Note: impedance has been normalized based on total positive electrode area of 1055 cm^2).

capacitance. On the other hand, the equivalent circuit for the negative electrode impedance spectra consists of two different time constants besides an inductor L and an ohmic resistance R_{ohm}. R_1 and CPE_1 for high-frequency arc are the resistance and corresponding capacitance related to the growth of SEI layer on the negative electrode, while R_2 and CPE_2 for low-frequency arc are the charge-transfer resistance and double-layer capacitance. The impedance spectrum of the negative electrode was fitted for the fresh cell only. It is very difficult to fit the impedance spectra for the negative electrode in the aged cells due to the complexity of their impedance data. Instead, charge-transfer resistance and total polarization resistance for the negative electrode in the case of aged cells were estimated directly from the impedance spectra.

The impedance spectra of the full cell, positive and negative electrodes for a fresh and two aged cells at −10°C (Figure 9) were fitted using above-mentioned equivalent circuits (Figure 10). The fitting parameter values are summarized in Table IV. The total resistance of cell/positive electrode at −10°C is dominated by charge-transfer resistance (R_2) rather than the resistance related to surface film on the positive electrode active materials (R_1), which is opposite to the case at 25°C. At 25°C (Figure 6 and Table III), the resistance related to surface film/electronic transport dominates the total resistance, especially for aged cells. When temperature is lowered from 25 to −10°C, the charge-transfer reaction kinetics at the electrodes becomes more sluggish, leading to a larger contribution of charge-transfer resistance to the total resistance of the cell/positive electrode. Moreover, for a fresh cell, the charge-transfer resistance of the full cell is much larger than that of positive electrode at −10°C, which implies that both positive and negative electrode contribute the charge-transfer resistance of the full cell, which is also quite different from the case at 25°C, in which the negative electrode shows little contribution to the charge-transfer resistance of the full cell (Figure 6). With lowering temperature from 25 to −10°C, both of the charge-transfer resistances of the positive and negative electrodes significantly increase. However, due to their different activation energies related to charge-transfer process, the charge-transfer resistance of the negative electrode increases more significantly with decreasing temperature than that of the positive electrode, leading to higher contribution of the negative electrode to the charge-transfer resistance of the full cells at lower temperature.

Figure 11 shows the ohmic resistance R_{ohm}, the resistances (R_1, R_{MF} and R_2) related to different processes, and total resistance of fresh and aged cells in the case of full cells and positive electrodes at −10°C. In the case of positive electrode impedance at −10°C, with increasing cycle number from 0 to 1500 cycles, the total resistance of the positive electrode increased by 142 Ω cm^2 (from 179 to 321 Ω cm^2). With regard to the resistances related to difference processes on the positive electrode at −10°C, the effect of aging is different. For example, from 0 to 1500 cycles, charge-transfer resistance (R_2) increased ~155 Ω cm^2 (from 58.3 to 213.6 Ω cm^2); and the resistance related to the surface film (R_1) increased by ~54 Ω cm^2 (from 7.63 to 61.6 Ω cm^2); while the electronic transport resistance (R_{MF}) decreased by ~70 Ω cm^2 (from 102.3 to 32.0 Ω cm^2). The increase R_1 is a result of growth of the surface film on the positive electrode active materials. Clearly, the significant increase in both charge-transfer resistance and the resistance related to the surface film on the positive electrode active materials are two main factors for the increase in total resistance of the positive electrode at −10°C. In the case of negative electrode impedance (Figure 9c and Table IV), very surprisingly, the total resistance of the negative electrode at −10°C decreases by ~32 Ω cm^2 (from 48.8 to 16.9 Ω cm^2) from 0 to 1500 cycles, which mainly comes from the decrease in its charge-transfer resistance. The decrease in the charge-transfer resistance on the negative electrode after aging may be related to the increase in electrochemical reaction area of negative electrode materials caused by the dramatic crack propagation of graphite negative electrode materials, which is consistent with the discharge performance of negative electrode in the thee-electrode cell (Figure 4d and Table I). At low temperatures such as −10°C, although the total resistance of the negative electrode decreases upon cycle aging, significant increase in the total resistance of the positive electrode upon cycle aging leads to a great increase in the total resistance of the full cell. For example, from 0 to 1500 cycles, the total cell resistance at −10°C increased by ~81 Ω cm^2 (from 242.1 to 323.1 Ω cm^2). Therefore, the power fade of the cell at low temperatures is mainly due to the impedance rise of positive electrode upon cycle aging, especially the rising charge-transfer resistance and the increasing resistance related to the surface film on the positive electrode active materials. Zhang et al.[17] investigated the aging behavior of Li-ion batteries with $LiNi_{0.8}Co_{0.15}Al_{0.05}O_2$ (NCA) positive electrode and graphite negative electrode and also found that the cell impedance rise comes mainly from the increase in the charge-transfer resistance and SEI layer resistance of the positive electrode.

Table IV. Fitting parameter values for the impedance spectra (excluding Warburg diffusion impedance) of a fresh and two aged cells (at 904 and 1500 cycles) measured at 80% SOC and −10°C in a three-electrode cell shown in Figure 9.

	Fresh			Aged, 904 cycles			Aged, 1500 cycles		
Cycle No.	cell	positive	negative	cell	positive	negative	cell	positive	negative
L (mH cm^2)	0.132	0.010	0.080	0.113	0.040	–	0.142	0.017	–
R_{ohm} (Ω cm^2)	10.90	10.94	0.23	12.9	10.5	–	14.3	13.8	–
R_1 (Ω cm^2)	7.35	7.63	2.76	39.6	38.4	–	61.4	61.6	–
CPE_1 A_1 (μF cm^{-2})	2.06	1.00	9.73	1.83	1.89	–	1.55	1.27	–
n_1	1.025	1.098	0.658	0.958	0.961	–	0.963	0.977	–
R_{MF} (Ω cm^2)	97.9	102.3	–	38.1	35.7	–	36.3	32.0	–
CPE_{MF} A_{MF} (mF cm^{-2})	6.01	4.48	–	2.16	1.69	–	1.95	1.31	–
n_{MF}	0.313	0.358	–	0.571	0.609	–	0.586	0.654	–
R_2 (Ω cm^2)	125.9	58.3	45.8	148.8	145.3	∼13.7*	211.1	213.6	∼15.8*
CPE_2 A_2 (mF cm^{-2})	1.85	1.48	6.17	6.63	7.85	–	6.11	6.81	–
n_2	0.754	0.904	1.056	0.915	0.915	–	0.920	0.939	–
R_{total} (Ω cm^2)	242.1	179.2	48.8	239.5	229.8	∼18.1*	323.1	321.0	∼16.9*

*Estimated by the ruler.

A comparison of cell performance measured in three- vs. two-electrode cells.—Figure 12 shows a comparison of the 1C charge-C/3 discharge performances of fresh and aged cells measured at room temperature (∼23°C) between in two and three-electrode cells. There is almost no difference in the cell performance for a fresh cell and an aged cell at 904 cycles. However, for an aged cell at 1500 cycles, the cell shows better C/3 discharge performance when measured in the three-electrode cell than in the two-electrode cell. For the same aged cell, similar results on 1C discharge performance were observed (Figures 4a and 4b). In general, a lithium-ion pouch cell is sealed under vacuum during cell fabrication and thus it is compact for an as-fabricated fresh cell. For a fresh cell, the contact of cell components is very intimate to reduce the contact resistance between cell components. However, during cell aging, SEI layer at the graphite negative electrode continuously grows with cycling, leading to the loss of lithium inventory and possible gas evolution due to the reaction of lithium and electrolyte solvents. In addition, for the cells studied in this work, significant lithium plating during the final stage of cycle life test occurs, leading to severe capacity fade (Figure 3). The deposited lithium on the surface of graphite negative electrode may also react with electrolyte solvents to thicken the SEI layer on the negative electrode and produce more gases. Recently, Matasso et al.[57,58] reported that gases are produced for a commercial lithium-ion cell with $LiCoO_2$/graphite electrode as products of the reduction of electrolyte solvents on the surface of negative electrode during SEI layer formation/growth and cracking formation/propagation, and identified that the gases generated during repeated cycling are CO, CO_2, CH_4, C_2H_6, and C_3H_8 using gas chromatograph-mass spectrometry (GC-MS) analysis. For the aged cell at 1500 cycles, swelling of the pouch cell can be obviously observed by an eye and the gases produced inside the pouch cell can be easily detected by touch. A large amount of gas decreases the electrode stack pressure, leading to the loss of the contact between cell components. Therefore, the aged cell at 1500 cycles shows much higher ohmic resistance than other aged cells at cycles of ≤1000 when measured in a two-electrode cell (Figure 5a). For a three-electrode cell, when the cell was assembled, the gases produced inside the pouch cell have been released and the pouch cell has been compressed by the setup. Moreover, the three-electrode pouch cells is soaked in a fresh electrolyte solution. Very interestingly, there is almost no change in the ohmic resistance among fresh and aged cells in a three-electrode cell (Figures 6a and 9a). For aged cells, lowering the ohmic resistance and strengthening the contact between cell components from two- to three-electrode cell together with the use of a fresh electrolyte solution in three-electrode cell lead to an improvement in cell performance (discharge capacity and power) measured in a three-electrode cell.

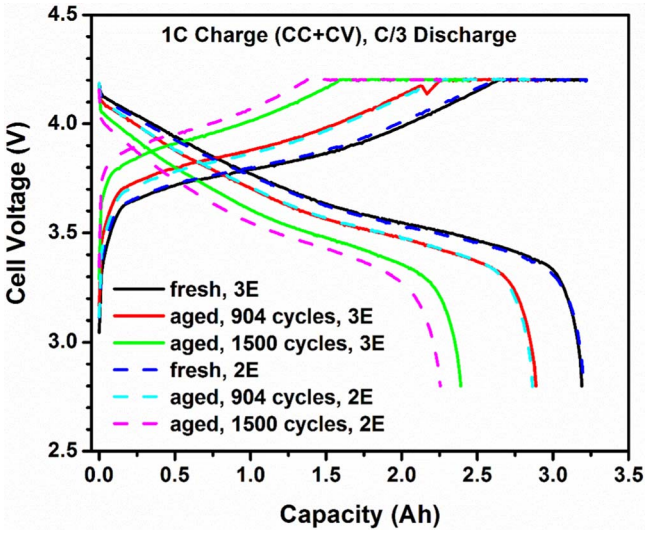

Figure 12. A comparison in 1C charge-C/3 discharge performance of fresh and aged cells measured at room temperature (∼23°C) between in three-electrode (3E) (solid lines) and two-electrode (2E) (dash lines) cells.

Conclusions

Capacity and power fade during cycle-life testing at room temperature were examined for high energy lithium-ion pouch cells with thick NMC622 cathodes and thick graphite anodes. The cells experience significant capacity and power fade upon aging. The cells exhibits a cycle life of ∼1419 cycles at capacity retention of ∼75%. Capacity fade is mainly due to the loss of lithium inventory, which is contributed to by two main factors: the growth of SEI layer and lithium plating. Power fade of the cell is mainly due to the degradation of the positive electrode including the growth of surface film on the positive electrode active materials and the increase in charge-transfer resistance. In order to further improve cycle life of high energy NMC622/graphite lithium-ion batteries, it is necessary to avoid lithium plating and prevent rapid growth of SEI layer on graphite anode during repeated cycling, and increase stability of NMC622 electrodes and active materials.

Acknowledgments

We greatly acknowledge BMW for financial support of this work and Umicore for cathode material support.

References

1. T. H. Kim, J. S. Park, S. K. Chang, S. Choi, J. H. Ryu, and H. K. Song, *Advanced Energy Materials*, **2**, 860 (2012).
2. W. Liu, P. Oh, X. Liu, M.-J. Lee, W. Cho, S. Chae, Y. Kim, and J. Cho, *Angewandte Chemie-International Edition*, **54**, 4440 (2015).
3. H. J. Noh, S. Youn, C. S. Yoon, and Y. K. Sun, *Journal of Power Sources*, **233**, 121 (2013).
4. C. Chae, H.-J. Noh, J. K. Lee, B. Scrosati, and Y.-K. Sun, *Advanced Functional Materials*, **24**, 3036 (2014).
5. Y.-K. Sun, S.-T. Myung, B.-C. Park, J. Prakash, I. Belharouak, and K. Amine, *Nature Materials*, **8**, 320 (2009).
6. A. Yamano, M. Morishita, M. Yanagida, and T. Sakai, *Journal of the Electrochemical Society*, **162**, A1730 (2015).
7. P. Rozier and J. M. Tarascon, *Journal of the Electrochemical Society*, **162**, A2490 (2015).
8. J. Qian, W. A. Henderson, W. Xu, P. Bhattacharya, M. Engelhard, O. Borodin, and J.-G. Zhang, *Nature Communications*, **6**, 6362 (2015).
9. Z. Liang, D. Lin, J. Zhao, Z. Lu, Y. Liu, C. Liu, Y. Lu, H. Wang, K. Yan, X. Tao, and Y. Cui, *Proceedings of the National Academy of Sciences of the United States of America*, **113**, 2862 (2016).
10. K. G. Gallagher, S. E. Trask, C. Bauer, T. Woehrle, S. F. Lux, M. Tschech, P. Lamp, B. J. Polzin, S. Ha, B. Long, Q. L. Wu, W. Q. Lu, D. W. Dees, and A. N. Jansen, *Journal of the Electrochemical Society*, **163**, A138 (2016).
11. J. Choi, B. Son, M.-H. Ryou, S. H. Kim, J. M. Ko, and Y. M. Lee, *Journal of Electrochemical Science and Technology*, **4**, 27 (2013).
12. H. Zheng, J. Li, X. Song, G. Liu, and V. S. Battaglia, *Electrochimica Acta*, **71**, 258 (2012).
13. M. Broussely, P. Biensan, F. Bonhomme, P. Blanchard, S. Herreyre, K. Nechev, and R. J. Staniewicz, *Journal of Power Sources*, **146**, 90 (2005).
14. J. Vetter, P. Novak, M. R. Wagner, C. Veit, K. C. Moller, J. O. Besenhard, M. Winter, M. Wohlfahrt-Mehrens, C. Vogler, and A. Hammouche, *Journal of Power Sources*, **147**, 269 (2005).
15. A. Barre, B. Deguilhem, S. Grolleau, M. Gerard, F. Suard, and D. Riu, *Journal of Power Sources*, **241**, 680 (2013).
16. T. Waldmann, N. Ghanbari, M. Kasper, and M. Wohlfahrt-Mehrens, *Journal of the Electrochemical Society*, **162**, A1500 (2015).
17. Y. Zhang and C.-Y. Wang, *Journal of the Electrochemical Society*, **156**, A527 (2009).
18. Y. Zhang, C.-Y. Wang, and X. Tang, *Journal of Power Sources*, **196**, 1513 (2011).
19. C. Snyder, C. Apblett, A. Grillet, T. Beechem, and D. Duquette, *Journal of the Electrochemical Society*, **163**, A1036 (2016).
20. T. Waldmann, M. Wilka, M. Kasper, M. Fleischhammer, and M. Wohlfahrt-Mehrens, *Journal of Power Sources*, **262**, 129 (2014).
21. M. Petzl, M. Kasper, and M. A. Danzer, *Journal of Power Sources*, **275**, 799 (2015).
22. A. M. Grillet, T. Humplik, E. K. Stirrup, S. A. Roberts, D. A. Barringer, C. M. Snyder, M. R. Janvrin, and C. A. Apblett, *Journal of the Electrochemical Society*, **163**, A1859 (2016).
23. M. Ecker, N. Nieto, S. Kaebitz, J. Schmalstieg, H. Blanke, A. Warnecke, and D. U. Sauer, *Journal of Power Sources*, **248**, 839 (2014).
24. S. F. Schuster, T. Bach, E. Fleder, J. Müller, M. Brand, G. Sextl, and A. Jossen, *Journal of Energy Storage*, **1**, 44 (2015).
25. K. Jalkanen, J. Karppinen, L. Skogstrom, T. Laurila, M. Nisula, and K. Vuorilehto, *Applied Energy*, **154**, 160 (2015).
26. S.-H. Lee, C. S. Yoon, K. Amine, and Y.-K. Sun, *Journal of Power Sources*, **234**, 201 (2013).
27. S. U. Woo, B. C. Park, C. S. Yoon, S. T. Myung, J. Prakash, and Y. K. Sun, *Journal of the Electrochemical Society*, **154**, A649 (2007).
28. S.-T. Myung, H.-J. Noh, S.-J. Yoon, E.-J. Lee, and Y.-K. Sun, *Journal of Physical Chemistry Letters*, **5**, 671 (2014).
29. H. Shi, X. Q. Wang, P. Y. Hou, E. L. Zhou, J. Guo, J. Zhang, D. G. Wang, F. X. Guo, D. W. Song, X. X. Shi, and L. Q. Zhang, *Journal of Alloys and Compounds*, **587**, 710 (2014).
30. E. M. Erickson, H. Bouzaglo, H. Sclar, K.-J. Park, B.-B. Lim, F. Schipper, C. Ghanty, J. Grinblat, B. Markovsky, Y.-K. Sun, and D. Aurbach, *Journal of the Electrochemical Society*, **163**, A1348 (2016).
31. Y.-K. Sun, Z. Chen, H.-J. Noh, D.-J. Lee, H.-G. Jung, Y. Ren, S. Wang, C. S. Yoon, S.-T. Myung, and K. Amine, *Nature Materials*, **11**, 942 (2012).
32. C.-Y. Wang, G. Zhang, S. Ge, T. Xu, Y. Ji, X.-G. Yang, and Y. Leng, *Nature*, **529**, 515 (2016).
33. C.-Y. Wang, T. Xu, S. Ge, G. Zhang, X.-G. Yang, and Y. Ji, *Journal of the Electrochemical Society*, **163**, A1944 (2016).
34. E. Sarasketa-Zabala, F. Aguesse, I. Villarreal, L. M. Rodriguez-Martinez, C. M. Lopez, and P. Kubiak, *Journal of Physical Chemistry C*, **119**, 896 (2015).
35. D. Aurbach, B. Markovsky, A. Rodkin, M. Cojocaru, E. Levi, and H. J. Kim, *Electrochimica Acta*, **47**, 1899 (2002).
36. M. Klett, R. Eriksson, J. Groot, P. Svens, K. C. Hogstrom, R. W. Lindstrom, H. Berg, T. Gustafson, G. Lindbergh, and K. Edstrom, *Journal of Power Sources*, **257**, 126 (2014).
37. S. S. Zhang, K. Xu, and T. R. Jow, *Electrochimica Acta*, **49**, 1057 (2004).
38. Y. Ji, Y. Zhang, and C.-Y. Wang, *Journal of the Electrochemical Society*, **160**, A636 (2013).
39. K. Shono, T. Kobayashi, M. Tabuchi, Y. Ohno, H. Miyashiro, and Y. Kobayashi, *Journal of Power Sources*, **247**, 1026 (2014).
40. E. McTurk, C. R. Birkl, M. R. Roberts, D. A. Howey, and P. G. Bruce, *Ecs Electrochemistry Letters*, **4**, A145 (2015).
41. I. Buchberger, S. Seidlmayer, A. Pokharel, M. Piana, J. Hattendorff, P. Kudejova, R. Gilles, and H. A. Gasteiger, *Journal of the Electrochemical Society*, **162**, A2737 (2015).
42. J. C. Burns, A. Kassam, N. N. Sinha, L. E. Downie, L. Solnickova, B. M. Way, and J. R. Dahn, *Journal of the Electrochemical Society*, **160**, A1451 (2013).
43. J. G. Xu, R. D. Deshpande, J. Pan, Y. T. Cheng, and V. S. Battaglia, *Journal of the Electrochemical Society*, **162**, A2026 (2015).
44. J. A. Gilbert, J. Bareño, T. Spila, S. E. Trask, D. J. Miller, B. J. Polzin, A. N. Jansen, and D. P. Abraham, *Journal of the Electrochemical Society*, **164**, A6054 (2016).
45. B. Stiaszny, J. C. Ziegler, E. E. Krauss, J. P. Schmidt, and E. Ivers-Tiffee, *Journal of Power Sources*, **251**, 439 (2014).
46. R. Deshpande, M. Verbrugge, Y. T. Cheng, J. Wang, and P. Liu, *Journal of the Electrochemical Society*, **159**, A1730 (2012).
47. M. Dubarry, C. Truchot, B. V. Liaw, K. Gering, S. Sazhin, D. Jamison, and C. Michelbacher, *Journal of Power Sources*, **196**, 10336 (2011).
48. M. B. Pinson and M. Z. Bazant, *Journal of the Electrochemical Society*, **160**, A243 (2013).
49. I. Bloom, S. A. Jones, V. S. Battaglia, G. L. Henriksen, J. P. Christophersen, R. B. Wright, C. D. Ho, J. R. Belt, and C. G. Motloch, *Journal of Power Sources*, **124**, 538 (2003).
50. M. Broussely, S. Herreyre, P. Biensan, P. Kasztejna, K. Nechev, and R. J. Staniewicz, *Journal of Power Sources*, **97-8**, 13 (2001).
51. T. Liu, A. Garsuch, F. Chesneau, and B. L. Lucht, *Journal of Power Sources*, **269**, 920 (2014).
52. Y. S. Lee, K. S. Lee, Y. K. Sun, Y. M. Lee, and D. W. Kim, *Journal of Power Sources*, **196**, 6997 (2011).
53. D. W. Dees, D. P. Abraham, W. Lu, K. G. Gallagher, M. Bettge, and A. N. Jansen, *Journal of the Electrochemical Society*, **162**, A559 (2015).
54. X. Y. Qiu, Q. C. Zhuang, Q. Q. Zhang, R. Cao, Y. H. Qiang, P. Z. Ying, and S. G. Sun, *Journal of Electroanalytical Chemistry*, **687**, 35 (2012).
55. Q. C. Zhuang, T. Wei, L. L. Du, Y. L. Cui, L. Fang, and S. G. Sun, *Journal of Physical Chemistry C*, **114**, 8614 (2010).
56. M. Itagaki, N. Kobari, S. Yotsuda, K. Watanabe, S. Kinoshita, and M. Ue, *Journal of Power Sources*, **135**, 255 (2004).
57. A. Matasso, D. Wetz, and F. Liu, *Journal of the Electrochemical Society*, **162**, A92 (2015).
58. A. Matasso, D. Wong, D. Wetz, and F. Liu, *Journal of the Electrochemical Society*, **161**, A2031 (2014).